Short Communication

# Impacts of ruthenium valence state on the electrocatalytic activity of ruthenium ion-complexed graphitic carbon nitride/reduced graphene oxide nanosheets towards hydrogen evolution reaction

Dingjie Pan [a], Qiming Liu [a], Forrest Nichols [a], Rene Mercado [a], Han-Lin Kuo [b], Jennifer Q. Lu [b], Frank Bridges [c], Shaowei Chen [a],*

[a] Department of Chemistry and Biochemistry, University of California, 1156 High Street, Santa Cruz, CA 95064, USA
[b] School of Engineering, University of California, 5200 North Lake Road, Merced, CA 95343, USA
[c] Department of Physics, University of California, 1156 High Street, Santa Cruz, CA 95064, USA

## HIGHLIGHTS

- Ruthenium atomically dispersed within $C_3N_4$/rGO nanosheets.
- Valence states manipulated by chemical reduction/oxidation.
- HER activity increases/decreases with electron-enrichment/depletion of Ru centers.
- Contribution of Ru 3d electrons to the density of states near the Fermi level.

## GRAPHICAL ABSTRACT
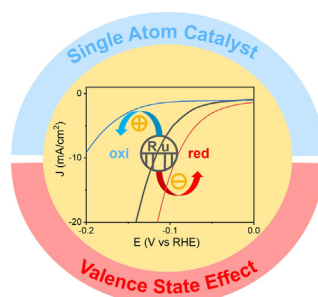


## ARTICLE INFO

## ABSTRACT

Design and engineering of effective electrode catalysts represents a critical first step for hydrogen production by electrochemical water splitting. Nanocomposites based on ruthenium atomically dispersed within a carbon scaffold have emerged as viable candidates. In the present study, ruthenium metal centers are atomically embedded within graphitic carbon nitride/reduced graphene oxide nanosheets by thermal refluxing. Subsequent chemical reduction/oxidation leads to ready manipulation of the ruthenium valence state, as evidenced in microscopic and spectroscopic measurements, and hence enhancement/diminishment of the electrocatalytic activity towards hydrogen evolution reaction in both acidic and alkaline media. This is largely ascribed to the increased/reduced contribution of the Ru valence electrons to the density of state near the Fermi level which dictates the binding and reduction of hydrogen. Results from this study highlight the significance of the valence state of metal centers in the manipulation and optimization of the catalytic performance of single atom catalysts.

## 1. Introduction

Hydrogen has been attracting extensive interest as a viable substitution of fossil fuels due to its remarkably high energy density (120 MJ kg$^{-1}$); yet, currently the commercial production of hydrogen is mostly based on catalytic reforming of natural gas, where $CO_2$ emissions are inevitable during the hydrogen generation process [1,2]. Producing hydrogen via electrochemical water splitting has emerged as an efficient and sustainable solution, which entails two half-reactions, hydrogen evolution reaction (HER) at the cathode and oxygen evolution reaction (OER) at the anode, where effi-

* Corresponding author.
  E-mail address: shaowei@ucsc.edu (S. Chen).

cient electrocatalysts are required to reduce the activation energy and overpotentials at both electrodes [3]. For an ideal HER catalyst, the Gibbs free energy of hydrogen adsorption ($\Delta G_H$) should be close to 0 eV, since weak hydrogen binding to the catalyst surface would limit the adsorption rate while strong binding would impede the desorption of the final product [4]. At present, platinum with a nearly thermo-neutral $\Delta G_H$ is considered as the catalyst of choice for HER. However, the natural scarcity and high cost of platinum renders it unsustainable to produce $H_2$ from water splitting based on platinum catalysts [5–7]. This has fuelled substantial research efforts of the development of cost-effective alternatives [8–13]. Within this context, ruthenium has been attracting extensive interest, due largely to a $\Delta G_H$ comparable to that of Pt but at ca. 60 % of the cost [14,15]. Remarkably, when ruthenium is atomically dispersed into a *N*-doped carbon matrix forming $RuC_xN_y$ moieties, the resulting composites exhibit a significant HER activity, as compared to commercial Pt/C [16–18]. For instance, in a previous study [16], refluxing of $RuCl_3$ with graphitic carbon nitride (g-$C_3N_4$) nanosheets led to the formation of $RuN_2$ moieties whereby Ru(III) was reduced to Ru(II) and chelated to the pyridinic N of two neighboring tri-s-triazine units (Ru-N). This intimate interaction between the Ru centers and the carbon scaffold led to substantial charge redistribution around the metal centers, where the adjacent Ru, N, and C atomic sites all exhibited a markedly reduced $|\Delta G_H|$ and collectively contributed to the binding and reduction of hydrogen. Further charge transfer from the metal centers could be achieved by the incorporation of reduced graphene oxide (rGO) nanosheets forming a stacked structure with the Ru-$C_3N_4$ composites (Ru-$C_3N_4$/rGO) [17]. Indeed, recent studies based on density functional theory (DFT) calculations have shown that the formation of g-$C_3N_4$/rGO heterostructures results in a reduced material bandgap [19–21]. Therefore, the strong electronic interactions among Ru, g-$C_3N_4$, and rGO improved the electrical conductivity and charge carrier density, and lowered the charge-transfer resistance, leading to additional enhancement of the HER performance [17]. This suggests that the valence state of the metal centers plays a critical role in dictating the HER activity.

Notably, the valence state of such single atom catalysts (SACs) has been recognized to exert a great impact on the electrocatalytic activity, since the adsorbate binding would be weakened with a decreasing density of valence-filling electrons [22–24]. This has been manifested in the manipulation of electrocatalytic activity towards a range of important reactions, such as HER, OER, and ORR (oxygen reduction reaction) [22,25–31]. For instant, Nichols et al. [28] embedded platinum centers into g-$C_3N_4$ nanosheets by refluxing with two different precursors ($PtCl_2$ and $PtCl_4$), and observed that the HER activity increased with increasing $Pt^{4+}$ concentration, with a low overpotential ($\eta_{10}$) of only −7.7 mV to reach the current density of 10 mA cm$^{-2}$ for the optimized sample. In another study [29], the valence state of the doping elements (Ir, Pt, and Ru) was found to impact the electrocatalytic activity of nickel–iron layer double hydroxide (NiFe-LDH). Specifically, compared to tetravalent iridium ($Ir^{4+}$), trivalent iridium ions ($Ir^{3+}$) showed a higher HER and OER activity, because the neighboring O atoms were electron-richer with the lower-valence $Ir^{3+}$ ion, which facilitated water dissociation and hydrogen desorption. A similar effect was also found with Ru and Pt ions, where $Pt^{2+}$ and $Ru^{3+}$ doped NiFe-LDH exhibited a better catalyst performance than that with $Pt^{4+}$ and $Ru^{4+}$. In another study [30], an enhanced HER performance was observed with high valence state Mo (i.e., $Mo^{4+}$, $Mo^{5+}$, and $Mo^{6+}$) in molybdenum carbide ($Mo_xC$), where oxidation of $Mo_xC$ nanoparticles by controlled air treatment led to improved HER activity in both acidic ($\eta_{10}$ = -130 mV) and alkaline media ($\eta_{10}$ = -116 mV). For Fe,*N*-codoped carbon composites [31], markedly better ORR and OER catalytic activities were observed at the $Fe^{2+}/Fe^{3+}$ ratio of 1.15 than at 1.5 and 0.92. Mechanistically, this

was accounted for by the synergistic interactions between the metal centers, where $Fe^{2+}$ facilitated oxygen adsorption and $Fe^{3+}$ was beneficial to the conduction of valence electrons of oxygen ions.

In this study, the ruthenium valence state of Ru-$C_3N_4$/rGO composites was manipulated by chemical reduction/oxidation, as manifested in X-ray spectroscopic measurements. The reduced sample was found to exhibit an enhanced HER activity in both acidic and alkaline media, whereas the performance diminished with the oxidized sample, as compared to the as-prepared composite. This was ascribed to the enhanced/diminished contribution of the Ru valence electrons for the reduced/oxidized nanocomposites to the density of state (DOS) near the Fermi level, which played a critical role in determining the energetics of hydrogen adsorption.

## 2. Experiment section

### 2.1. Chemicals

Melamine (99 %, Acros), ruthenium(III) chloride hydrate ($RuCl_3$·$xH_2O$, 35–40 % Ru, Acros), graphite flakes (Fisher Chemicals), sulfuric acid ($H_2SO_4$, 98 %, Fisher Chemicals), potassium hydroxide (KOH, 99 %, Acros), sodium nitrate ($NaNO_3$, 99 %, Acros), potassium permanganate ($KMnO_4$, 99 %, Fisher Chemicals), sodium borohydride ($NaBH_4$, 99 %, Acros), and ascorbic acid (99 %, Fisher Chemicals) were used as received without further purification. Deionized water was supplied with a Barnstead Nanopure Waster System (18.2 MΩ cm).

### 2.2. Sample preparation

The synthesis of Ru-$C_3N_4$/rGO nanocomposites was detailed previously [17]. In brief, 10 g of melamine was heated in a muffle oven at 600 °C for 3 h in a covered crucible. The obtained g-$C_3N_4$ sample was then ground to a fine powder.

The modified Hummers method was used in the synthesis of graphene oxide (GO) nanosheets. Experimentally, 2 g of graphite and 1 g of $NaNO_3$ were ground and transferred to a 1000 mL round-bottom flask in an ice bath. 46 mL of concentrated $H_2SO_4$ and 6 g of $KMnO_4$ were added slowly into the flask under magnetic stirring for 3 h. The flask was then heated at 35 °C in an oil bath under stirring with the addition of 92 mL of $H_2O$, and further heated at 95 °C for 30 min. After the solution was cooled down to ambient temperature, 150 mL of $H_2O$ and 20 mL of $H_2O_2$ were added slowly into the flask, followed by 50 mL of concentrated HCl and 300 mL of $H_2O$ before centrifugation. The supernatant was collected and neutralized with $NaHCO_3$ to pH ≈ 7 before being dialyzed for 7 d (with a daily change of water) and finally freeze-dried.

To prepare g-$C_3N_4$/rGO composites, 100 mg of the g-$C_3N_4$ powders prepared above was dispersed into 100 mL of Nanopure water under sonication in a round-bottom flask for 1 h, into which was then added 100 mg of the above-obtained GO nanosheets. After sonication for 1 h, 352 mg of ascorbic acid was added into the solution, which was refluxed in an oil bath at 100 °C for 2 h. The resultant g-$C_3N_4$/rGO composites were collected by centrifugation for 10 min and dried overnight.

To incorporate Ru centers into g-$C_3N_4$/rGO, the g-$C_3N_4$/rGO hybrids prepared above were dispersed in 100 mL of Nanopure water under sonication for 1 h, into which was then added 56 mg of $RuCl_3$. The mixture was refluxed at 100 °C in an oil bath for 2 h. The Ru-$C_3N_4$/rGO composites were collected by centrifugation for 10 min and rinsed with $H_2O$ and ethanol two times.

The valence state of Ru in the Ru-$C_3N_4$/rGO composites was further manipulated by chemical reduction/oxidation. In the reduc-

tion process, 20 mg of Ru-C$_3$N$_4$/rGO was dispersed into 4 mL of H$_2$O, into which was added freshly prepared 1 mL of a NaBH$_4$ solution (3 mg mL$^{-1}$). The mixture was under magnetic stirring for 30 min before the solid was collected by centrifugation and dried overnight. The resulting sample was denoted as Ru-C$_3$N$_4$/rGO$_{red}$. The oxidation treatment was carried out in a similar fashion except that 1 mL of a KMnO$_4$ solution (8.8 mg mL$^{-1}$) was used instead, and the resulting sample was referred to as Ru-C$_3$N$_4$/rGOox.

### 2.3. Characterization

Transmission electron microscopy (TEM) measurements were carried out with an FEI Tecnai G2 200 kV TEM. Elemental mapping analyses based on energy-dispersive X-ray spectroscopy (EDS) were carried out with a Talos F200C G2 TEM. Scanning electron microscopic (SEM) studies, along with element mapping analysis, were conducted with a Thermo Fisher Scientific Apreo S LoVac electron microscope. X-ray photoelectron spectroscopic (XPS) studies were performed with a Thermo Scientific K-Alpha X-ray Photoelectron Spectrometer. X-ray diffraction (XRD) patterns were acquired with a Rigaku Smartlab Diffractometer. X-ray absorption spectroscopy (XAS) measurements were carried out at 10 K at beamline 4–1 of the Stanford Synchrotron Radiation Light source using an Oxford liquid helium cryostat.

### 2.4. Electrochemistry

Electrochemical measurements were carried out with a CHI 710 electrochemical workstation, while electrochemical impedance spectroscopy (EIS) and Mott-Schottky tests were conducted with a Gamry Reference 600 instrument. A glassy carbon rotating disk electrode (RDE, surface area 0.196 cm$^2$) and a graphite rod were used as the working electrode and counter electrode, respectively. The Ag/AgCl reference electrode (in 3 M KCl) was calibrated against a reversible hydrogen electrode (RHE), and all potentials in the present study were referenced to this RHE. To prepare catalyst inks, 2 mg of the nanocomposite catalysts obtained above and 3 mg of Vulcan XC72 carbon black were dispersed in a mixture of H$_2$O (200 μL), ethanol (790 μL) and Nafion (10 μL). After sonication for 30 min, 15 μL of the ink was dropcast evenly onto the RDE surface. The electrode was dried at ambient temperature before being immersed into an electrolyte solution for electrochemical measurements. All measurements were repeated at least 2 times and the deviations were typically under 5 %.

## 3. Results and discussion

Experimentally, g-C$_3$N$_4$ nanosheets were derived thermally from melamine, and GO from chemical exfoliation of graphite flakes. The stacked structure of g-C$_3$N$_4$/rGO hybrids was then prepared by refluxing the g-C$_3$N$_4$ and GO mixture in the presence of ascorbic acid [32,33]. A second thermal refluxing with RuCl$_3$ led to the incorporation of ruthenium centers via chelation to the pyridinic nitrogen of the tri-s-triazine units of the g-C$_3$N$_4$/rGO scaffold, forming Ru-C$_3$N$_4$/rGO nanocomposites [16,17]. The valence state of the Ru centers was further manipulated by NaBH$_4$ reduction or KMnO$_4$ oxidation, producing Ru-C$_3$N$_4$/rGO$_{red}$ and Ru-C$_3$N$_4$/rGO$_{ox}$, respectively.

The sample structures were first characterized by TEM measurements. From Fig. 1**a**, the as-prepared Ru-C$_3$N$_4$/rGO sample can be seen to exhibit a flaky nanosheet morphology [17]. In high-resolution TEM measurements (Fig. 1**b**), one can see that the sample consisted of arrays of nanocrystalline domains (ca. 2 nm) with a slightly darker contrast against a largely amorphous (light grey) background, and exhibited well-defined lattice fringes

with an interplanar distance of 0.237 nm that can be ascribe to the (110) crystalline planes of g-C$_3$N$_4$ [34], indicative of successful stacking of C$_3$N$_4$ onto rGO nanosheets, mostly due to π-π interactions between the two-dimensional nanosheets [17]. No obvious lattice fringes can be assigned to either metallic Ru or RuO$_2$, suggesting atomically dispersed Ru within the C$_3$N$_4$/rGO scaffold (further confirmation by XPS and XAS measurements, vide infra). Consistent results were obtained from EDS-based elemental mapping analysis. From Fig. 1**c**, the element of Ru can be readily identified, yet only discretely within the sample matrix, consistent with the atomic dispersion of ruthenium within the carbon matrix [17]. Notably, no apparent variation of the sample structure and elemental distributions was observed after chemical reduction or oxidation (**Figure S1 and S2**). Similar results were obtained from SEM and EDS measurements. From **Figure S3-S5**, one can see a rather consistent distribution pattern for C, N, and O, although it was apparently different from that of Ru, in agreement with the stacking interaction between g-C$_3$N$_4$ and rGO nanosheets (and the absence of RuO$_2$).

The corresponding XRD patterns are shown in **Figure S6**. The main diffraction peak at 2θ = 27.5° can be ascribed to the combined contributions of C$_3$N$_4$ (002) and rGO (002) facets [16,35–38]. It should be noted that no peaks can be resolved for metallic Ru or RuO$_x$ nanoparticles, consistent with the atomic dispersion of Ru in the sample [17].

The chemical composition and valence states of the composites were determined by XPS measurements. From the survey spectra in **Figure S7a**, the C 1 s/Ru 3d, N 1 s, Ru 3p, and O 1 s electrons can be readily identified at ca. 284, 400, 475, and 532 eV for the sample series. On the basis of the integrated peak areas, the elemental contents of Ru-C$_3$N$_4$/rGO were estimated to be 69.48 at.% for C, 13.21 at.% for N, 15.10 at.% for O, and 2.22 at.% for Ru [17]. The high-resolution scans of the Ru 3p electrons are shown in Fig. 2**a** (the right panel is the zoom in of the Ru 3p$_{3/2}$ peaks). Deconvolution yields two doublets for all three samples (**Table S1**). For Ru-C$_3$N$_4$/rGO, the doublet at 463.30/485.50 eV can be assigned to the 3p$_{3/2}$/3p$_{1/2}$ electrons of Ru(II), and the other at 465.81/488.01 eV to Ru(III). The binding energies diminished slightly for the Ru-C$_3$N$_4$/rGO$_{red}$, Ru(II) at 462.98/485.24 eV and Ru(III) at 465.14/487.30 eV, whereas a small increase was observed with Ru-C$_3$N$_4$/rGO$_{ox}$, Ru(II) at 463.52/485.65 eV and Ru(III) at 465.93/487.83 eV [16,17]. This suggests effective electron-enrichment/depletion of the Ru centers by postsynthesis chemical reduction/oxidation. In addition, the fact that no metallic Ru was detected in the samples was consistent with atomic dispersion of Ru into the carbon scaffold, as suggested in the above TEM and XRD measurements.

The corresponding C 1 s and Ru 3d spectra are shown in **Figure S7b**, where a rather appreciable change of the Ru 3d$_{5/2}$ binding energy can also be observed, Ru-C$_3$N$_4$/rGO$_{red}$ (281.73 eV) < Ru-C$_3$N$_4$/rGO (281.85 eV) < Ru-C$_3$N$_4$/rGO$_{ox}$ (282.09 eV), in good agreement with the trend of the Ru 3p electrons. In addition, the N-C=N and C=C peaks can be identified at ca. 288.0 and 284.5 eV, respectively [16,17], and remained virtually unchanged after chemical reduction/oxidation, suggesting minimal impacts on the carbon scaffold. Similar behaviors were observed in the relevant N 1 s and O 1 s spectra (**Figure S7c-d and Table S1**). The fact that no peak below 530 eV can be resolved in the O 1 s spectra suggests the absence of Ru-O species in the samples, and Ru was most likely chelated to N (and C), in good agreement with results from XAS measurements, as shown below.

Further structural insights were obtained from XAS measurements. From the Ru K-edge X-ray absorption near-edge structure (XANES) spectra in Fig. 2b, one can see that the absorption edges of the samples all lie in the intermediate between those of Ru foil and RuO$_2$, suggesting a valence state between 0 and + 4, which is
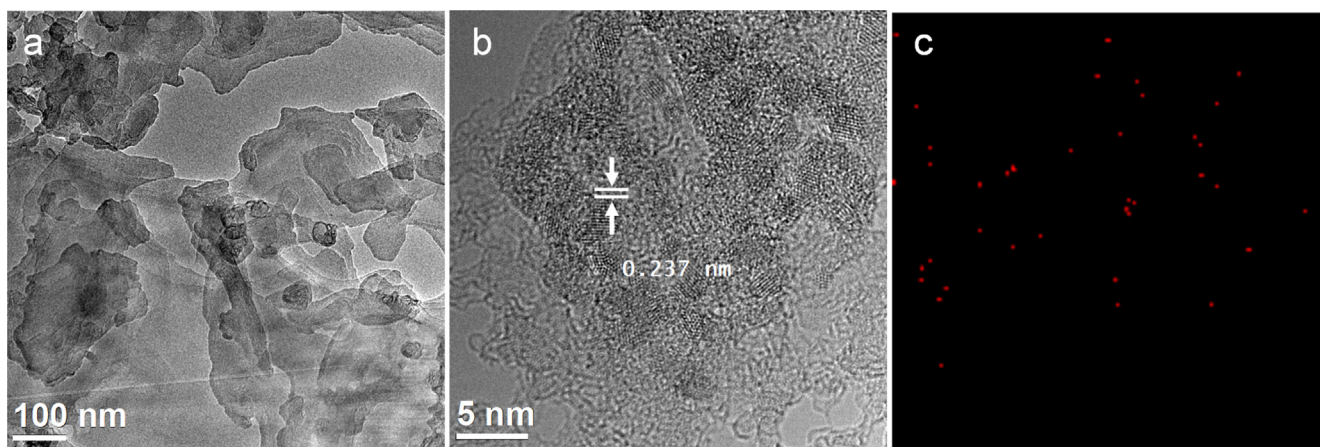
**Fig. 1.** (a,b) TEM images of Ru-C₃N₄/rGO at different magnifications. Scale bars are (a) 100 nm and (b) 5 nm. (c) The corresponding elemental map of Ru.
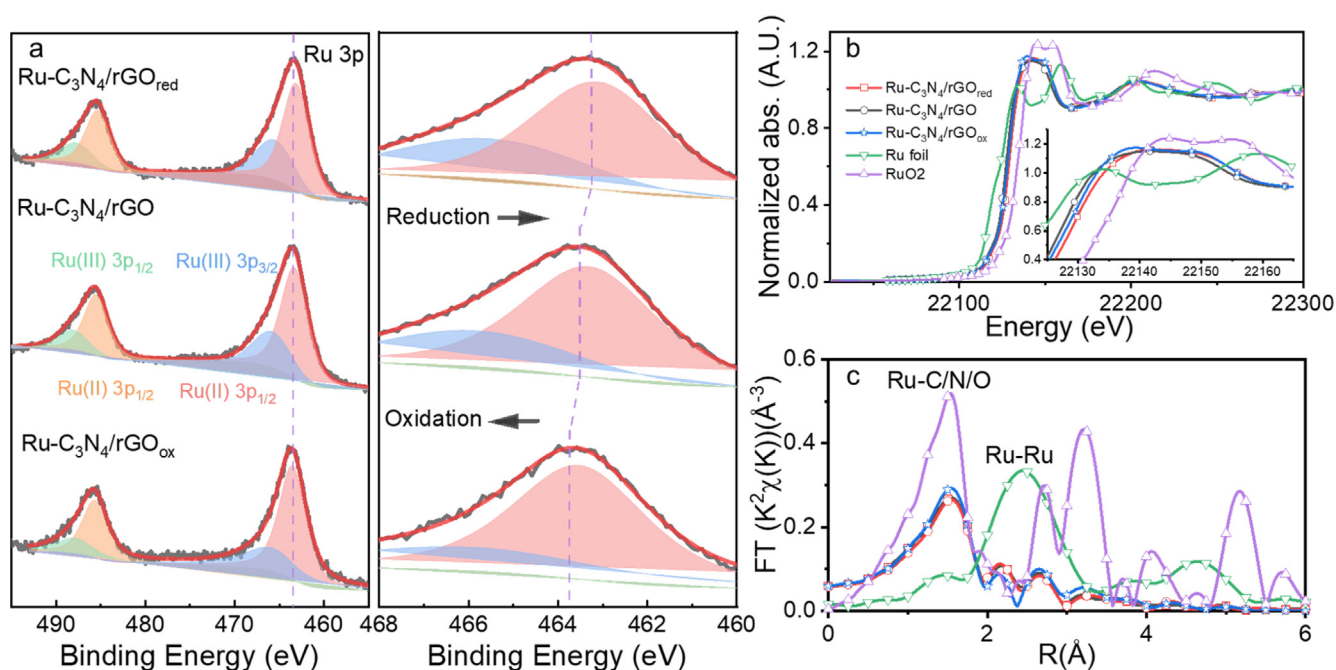


**Fig. 2.** (a) (left panel) XPS spectra of Ru 3p electrons of Ru-C₃N₄/rGO$_{red}$, Ru-C₃N₄/rGO, and Ru-C₃N₄/rGO$_{ox}$, with the sp$_{3/2}$ peaks magnified in the right panel to highlight the shift of the binding energy. (b) Normalized Ru K-edge XANES spectra of Ru-C₃N₄/rGO$_{red}$, Ru-C₃N₄/rGO, Ru-C₃N₄/rGO$_{ox}$, and the standard Ru foil and RuO₂. Inset is the zoom in of the area near the absorption edge. (c) Ru K-edge R-space EXAFS data for the corresponding samples within the Fourier transformation range of 3.5 to 11 Å$^{-1}$.

consistent with the atomic dispersion of Ru(II)/Ru(III) centers within the carbon skeleton. In addition, from the inset to Fig. 2b, one can see that the absorption edge energy varied in the order of Ru-C₃N₄/rGO$_{red}$ ≈ Ru-C₃N₄/rGO < Ru-C₃N₄/rGO$_{ox}$, in agreement with results from the XPS measurements where chemical reduction/oxidation led to electron-enrichment/depletion of the Ru centers.

Notably, the extended X-ray absorption fine structures (EXAFS) of the composite samples also exhibited a clear deviation from those of Ru foil and RuO₂, further confirming the absence of metal Ru and RuO₂ nanoparticles in the samples; and the almost identical oscillation patterns suggest a consistent atomic configuration that was retained during chemical reduction/oxidation.

The corresponding R-space EXAFS data are depicted in Fig. 2c (the k-space plot is shown in **Figure S8**), where the nanocomposites of Ru-C₃N₄/rGO$_{red}$, Ru-C₃N₄/rGO and Ru-C₃N₄/rGO$_{ox}$ all exhibited only a major peak at 1.5 Å, which is characteristic of the Ru-C/

N/O bonds [18]. However, as no Ru-O linkage was identified in XPS measurements (Figure S7 and Table S1), the Ru centers were embedded within the carbon scaffold most likely via the Ru-C/N bonds only. Note that this peak (1.5 Å) is very prominent with the RuO₂ reference, which also included a series of additional peaks above 2.5 Å for the Ru-Ru paths. The fact that the latter can not be found in the nanocomposites suggests the absence of RuO₂ nanoparticles in the samples. In addition, the Ru foil exhibited a major peak at 2.3 Å for the Ru-Ru bond, which is also absent in the nanocomposites. Taken together, these observations are in excellent agreement with results from TEM, XPS, and XRD measurements that no Ru or RuO$_x$ nanoparticles were produced in the nanocomposites and ruthenium was atomically dispersed into the matrix forming RuC$_x$N$_y$ moieties. Furthermore, the Ru-C/N configuration was determined by fitting of the EXAFS data (Fig. 2c and S8), which featured an almost identical bond length and coordination number among the three samples, 2.03 Å and 5.56 for Ru-

$C_3N_4/rGO_{red}$, 2.03 Å and 5.00 for Ru-$C_3N_4/rGO$, and 2.02 Å and 6.31 for Ru-$C_3N_4/rGO_{ox}$ (**Table S2**) [39–41]. That is, the coordination environment of the Ru centers remained largely invariant before and after chemical reduction/oxidation of the samples.

The HER performance of the sample series was then examined and compared in 0.5 M $H_2SO_4$. From the polarization curves in Fig. 3**a**, one can see that in comparison to the as-prepared Ru-$C_3N_4/rGO$, chemical reduction (oxidation) drastically enhanced (diminished) the HER activity, as manifested by the significant variation of the corresponding $\eta_{10}$, in the order of Ru-$C_3N_4/rGO_{ox}$ (-205 mV) < Ru-$C_3N_4/rGO$ (-130 mV) < Ru-$C_3N_4/rGO_{red}$ (-93 mV). The Tafel plots are depicted in Fig. 3**b**, where the Tafel slope varied in the order of Ru-$C_3N_4/rGO_{ox}$ (99.08 mV dec$^{-1}$) > Ru-$C_3N_4/rGO$ (75.78 mV dec$^{-1}$) $\geq$ Ru-$C_3N_4/rGO_{red}$ (75.64 mV dec$^{-1}$), suggesting enhanced (impeded) electron-transfer kinetics by chemical reduction (oxidation), although the performance remained subpar as compared to commercial Pt/C, which featured an $\eta_{10}$ of $-34$ mV and a Tafel slope of 17.35 mV dec$^{-1}$. This is also confirmed in electrochemical impedance spectroscopy measurements. From the Nyquist plots acquired at $-100$ mV (Fig. 3**c**), the charge-transfer resistance ($R_{ct}$, **Table S3**) can be found to decrease markedly in the order of Ru-$C_3N_4/rGO_{ox}$ (678 Ω) > Ru-$C_3N_4/rGO$ (39 Ω) > Ru-$C_3N_4/rGO_{red}$ (18 Ω). Notably, similar results were obtained in 1 M KOH, in terms of $\eta_{10}$, Tafel slope and $R_{ct}$ (**Figure S9** and **Table S3**).

Mechanistically, results from first principles calculations [16] have shown that the incorporation of Ru centers within g-$C_3N_4$ led to an apparent redistribution of electrons within the composite, and hence an enhanced density of states (DOS) at the Fermi level, which dictates the adsorption and reduction of hydrogen, as compared to the pristine g-$C_3N_4$, with the Ru 4d and 5 s orbitals being the major contributors. This will be strengthened (weakened) when the ruthenium centers are chemically reduced (oxidized), as manifested in the change of valence state by XPS measurements, electrical conductivity by electrochemical impedance measurements, and HER activity in both acidic and alkaline media by electrochemical measurements.

Remarkably, the Ru-$C_3N_4/rGO_{red}$ sample also exhibited excellent stability. From the chronoamperometric tests conducted at $-125$ mV in Fig. 3**d**, one can see that the voltametric currents were highly reproducible for up to 9 h when the hydrogen bubbles were removed every 3 h from the RDE surface.

## 4. Conclusions

In summary, Ru-$C_3N_4/rGO$ ternary nanocomposites were prepared by a facile wet-chemistry procedure. Chemical reduction/oxidation led to a ready variation of the valence state of the ruthenium metal centers, whereas the carbon scaffolds remained largely intact, as manifested in microscopic and spectroscopic measurements. Remarkably, the HER performances in both acidic and alkaline media were found to enhance (diminish) drastically after chemical reduction (oxidation), in comparison to the as-produced sample. The correlation of electron-enriched (-deficient) Ru centers with markedly enhanced (diminished) HER activity suggested an increased (reduced) contribution of Ru valence electrons to the DOS near the Fermi level that dictated the energetics of hydrogen adsorption. Results from this study may be exploited as a unique strategy for the deliberate structural
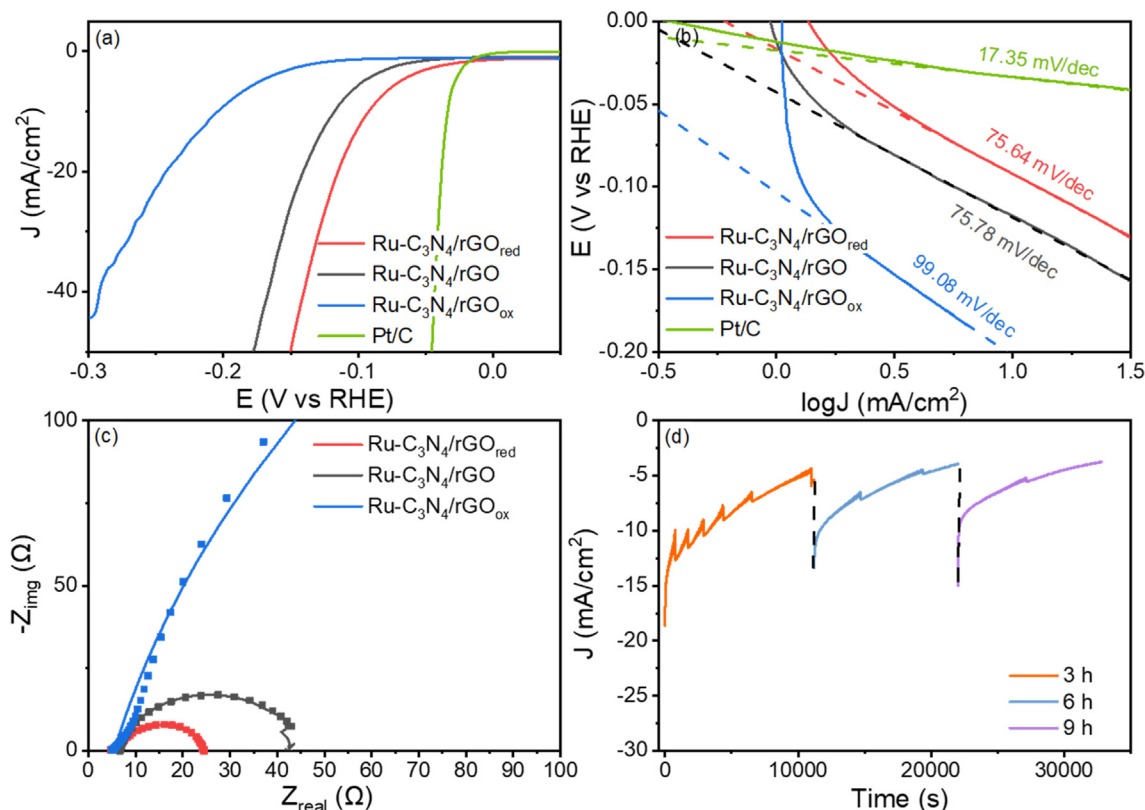


**Fig. 3.** (a) HER polarization curves of Ru-$C_3N_4/rGO_{red}$, Ru-$C_3N_4/rGO$, Ru-$C_3N_4/rGO_{ox}$ and commercial Pt/C in 0.5 M $H_2SO_4$, and (b) the Corresponding Tafel plots. (c) Nyquist plots of the samples without carbon black at $-100$ mV in 0.5 M $H_2SO_4$. Inset is the equivalent circuit where $R_s$ is the serial resistance, CPE is the constant phase element and $R_{ct}$ is the charge-transfer resistance. (d) Chronoamperometric measurements of Ru-$C_3N_4/rGO_{red}$ applying $-125$ mV in 0.5 M $H_2SO_4$ for 9 h, where hydrogen bubbles are removed from the RDE surface every 3 h.

engineering of single atom catalysts and ultimate optimization of their electrocatalytic activity [23].

## CRediT authorship contribution statement

**Dingjie Pan:** Data curation, Formal analysis, Methodology, Writing – original draft. **Qiming Liu:** Data curation, Formal analysis. **Forrest Nichols:** Data curation. **Rene Mercado:** Data curation. **Han-Lin Kuo:** Data curation. **Jennifer Q. Lu:** Data curation. **Frank Bridges:** Data curation, Formal analysis, Funding acquisition. **Shaowei Chen:** Conceptualization, Methodology, Validation, Formal analysis, Resources, Project administration, Funding acquisition, Writing – review & editing.

## Data availability

Data will be made available on request.

## Declaration of Competing Interest

The authors declare that they have no known competing financial interests or personal relationships that could have appeared to influence the work reported in this paper.

## Acknowledgments

## Appendix A. Supplementary data

Supplementary data to this article can be found online at https://doi.org/10.1016/j.jcis.2022.09.080.

## References

[1] F. Dawood, M. Anda, G.M. Shafiullah, Hydrogen production for energy: An overview, Int J Hydrog Energy 45 (7) (2020) 3847–3869.

[2] J. Yu, Q. He, G. Yang, W. Zhou, Z. Shao, M. Ni, Recent Advances and Prospective in Ruthenium-Based Materials for Electrochemical Water Splitting, ACS Catal 9 (11) (2019) 9973–10011.

[3] B. Xiong, L. Chen, J. Shi, Anion-containing noble-metal-free bifunctional electrocatalysts for overall water splitting, ACS Catal 8 (4) (2018) 3688–3707.

[4] Z.W. Seh, J. Kibsgaard, C.F. Dickens, I.b. Chorkendorff, J.K. Nørskov, T.F. Jaramillo, Combining theory and experiment in electrocatalysis: Insights into materials design, Science 355 (6321) (2017).

[5] P. Du, R. Eisenberg, Catalysts made of earth-abundant elements (Co, Ni, Fe) for water splitting: Recent progress and future challenges, Energy, Environ Sci 5 (2012) 6012–6021.

[6] C.C.L. McCrory, S. Jung, I.M. Ferrer, S.M. Chatman, J.C. Peters, T.F. Jaramillo, Benchmarking hydrogen evolving reaction and oxygen evolving reaction electrocatalysts for solar water splitting devices, J Am Chem Soc 137 (13) (2015) 4347–4357.

[7] S.J.A. Moniz, S.A. Shevlin, D.J. Martin, Z.-X. Guo, J. Tang, Visible-light driven heterojunction photocatalysts for water splitting–a critical review, Energy, Environ Sci 8 (3) (2015) 731–759.

[8] H.I. Karunadasa, E. Montalvo, Y. Sun, M. Majda, J.R. Long, C.J. Chang, A molecular MoS2 edge site mimic for catalytic hydrogen generation, Science 335 (6069) (2012) 698–702.

[9] J. Kibsgaard, Z. Chen, B.N. Reinecke, T.F. Jaramillo, Engineering the surface structure of MoS 2 to preferentially expose active edge sites for electrocatalysis, Nat Mater 11 (2012) 963–969.

[10] B. Cao, G.M. Veith, J.C. Neuefeind, R.R. Adzic, P.G. Khalifah, Mixed close-packed cobalt molybdenum nitrides as non-noble metal electrocatalysts for the hydrogen evolution reaction, J Am Chem Soc 135 (51) (2013) 19186–19192.

[11] X. Hu, B.S. Brunschwig, J.C. Peters, Electrocatalytic hydrogen evolution at low overpotentials by cobalt macrocyclic glyoxime and tetraimine complexes, J Am Chem Soc 129 (29) (2007) 8988–8998.

[12] P.-A. Jacques, V. Artero, J. Pécaut, M. Fontecave, Cobalt and nickel diimine-dioxime complexes as molecular electrocatalysts for hydrogen evolution with low overvoltages, Proc Natl Acad Sci 106 (49) (2009) 20627–20632.

[13] S.W. Kohl, L. Weiner, L. Schwartsburd, L. Konstantinovski, L.J.W. Shimon, Y. Ben-David, M.A. Iron, D. Milstein, Consecutive thermal H2 and light-induced O2 evolution from water promoted by a metal complex, Science 324 (5923) (2009) 74–77.

[14] N. Wang, S.L. Ning, X.L. Yu, D. Chen, Z.L. Li, J.C. Xu, H. Meng, D.K. Zhao, L.G. Li, Q. M. Liu, B.Z. Lu, S.W. Chen, Graphene composites with Ru-RuO2 heterostructures: Highly efficient Mott-Schottky-type electrocatalysts for pH-universal water splitting and flexible zinc-air batteries, Appl Catal B-Environ, 302 (2022) 120838.

[15] Q. Liu, B. Lu, F. Nichols, J. Ko, R. Mercado, F. Bridges, S. Chen, Rapid preparation of carbon-supported ruthenium nanoparticles by magnetic induction heating for efficient hydrogen evolution reaction in both acidic and alkaline media, SusMat 2 (3) (2022) 335–346.

[16] Y.i. Peng, B. Lu, L. Chen, N. Wang, J.E. Lu, Y. Ping, S. Chen, Hydrogen evolution reaction catalyzed by ruthenium ion-complexed graphitic carbon nitride nanosheets, J Mater Chem A 5 (34) (2017) 18261–18269.

[17] Y.i. Peng, W. Pan, N. Wang, J.-E. Lu, S. Chen, Ruthenium Ion-Complexed Graphitic Carbon Nitride Nanosheets Supported on Reduced Graphene Oxide as High-Performance Catalysts for Electrochemical Hydrogen Evolution, Chemsuschem 11 (1) (2018) 130–136.

[18] B.Z. Lu, L. Guo, F. Wu, Y. Peng, J.E. Lu, T.J. Smart, N. Wang, Y.Z. Finfrock, D. Morris, P. Zhang, N. Li, P. Gao, Y. Ping, S.W. Chen, Ruthenium atomically dispersed in carbon outperforms platinum toward hydrogen evolution in alkaline media, Nat Commun 10 (2019) 631.

[19] M. Yan, Q. Jiang, Lu. Yang, H. He, H. Huang, Three-Dimensional Ternary Hybrid Architectures Constructed from Graphene, MoS2, and Graphitic Carbon Nitride Nanosheets as Efficient Electrocatalysts for Hydrogen Evolution, ACS Appl Energy Mater 3 (7) (2020) 6880–6888.

[20] H. He, Y. Chen, C. Yang, L. Yang, Q. Jiang, H. Huang, Constructing 3D interweaved MXene/graphitic carbon nitride nanosheets/graphene nanoarchitectures for promoted electrocatalytic hydrogen evolution, J Energy Chem 67 (2022) 483–491.

[21] H. Huang, M. Yan, C. Yang, H. He, Q. Jiang, L. Yang, Z. Lu, Z. Sun, X. Xu, Y. Bando, Y. Yamauchi, Graphene Nanoarchitectonics: Recent Advances in Graphene-Based Electrocatalysts for Hydrogen Evolution Reaction, Adv Mater 31 (2019) 1903415.

[22] S. Kim, C. Choi, J. Hwang, J. Park, J. Jeong, H. Jun, S. Lee, S.-K. Kim, J.H. Jang, Y. Jung, Interaction mediator assisted synthesis of mesoporous molybdenum carbide: Mo-valence state adjustment for optimizing hydrogen evolution, ACS nano 14 (2020) 4988–4999.

[23] B.Z. Lu, Q.M. Liu, S.W. Chen, Electrocatalysis of Single-Atom Sites: Impacts of Atomic Coordination, Acs Catal 10 (2020) 7584–7618.

[24] Y.X. Wang, H.Y. Su, Y.H. He, L.G. Li, S.Q. Zhu, H. Shen, P.F. Xie, X.B. Fu, G.Y. Zhou, C. Feng, D.K. Zhao, F. Xiao, X.J. Zhu, Y.C. Zeng, M.H. Shao, S.W. Chen, G. Wu, J. Zeng, C. Wang, Advanced Electrocatalysts with Single-Metal-Atom Active Sites, Chem Rev 120 (2020) 12217–12314.

[25] Y. Tian, L. Cao, P. Qin, Bimetal– Organic Framework Derived High-Valence-State Cu-Doped Co3O4 Porous Nanosheet Arrays for Efficient Oxygen Evolution and Water Splitting, ChemCatChem 11 (2019) 4420–4426.

[26] P. Guo, Z. Wang, T. Zhang, C. Chen, Y. Chen, H. Liu, M. Hua, S. Wei, X. Lu, Initiating an efficient electrocatalyst for water splitting via valence configuration of cobalt-iron oxide, Appl Catal B: Environ 258 (2019) 117968.

[27] Q. Liu, H. Wang, X. Wang, R. Tong, X. Zhou, X. Peng, H. Wang, H. Tao, Z. Zhang, Bifunctional Ni1− xFex layered double hydroxides/Ni foam electrodes for high-efficient overall water splitting: A study on compositional tuning and valence state evolution, Int J Hydrog Energy 42 (2017) 5560–5568.

[28] F. Nichols, J.E. Lu, R. Mercado, R. Dudschus, F. Bridges, S.W. Chen, Platinum Oxide Nanoparticles for Electrochemical Hydrogen Evolution: Influence of Platinum Valence State, Chem-Eur J 26 (2020) 4136–4142.

[29] M. Wang, J.Q. Wang, C. Xi, C.Q. Cheng, C.G. Kuai, X.L. Zheng, R. Zhang, Y.M. Xie, C.K. Dong, Y.J. Chen, Valence-State Effect of Iridium Dopant in NiFe (OH) 2 Catalyst for Hydrogen Evolution Reaction, Small 17 (2021) 2100203.

[30] P. Wang, J. Qi, X. Chen, C. Li, T. Wang, C. Liang, New insights into high-valence state Mo in molybdenum carbide nanobelts for hydrogen evolution reaction, Int J Hydrog Energy 42 (2017) 10880–10890.

[31] X.-T. Wu, L.-J. Peng, K. Xiao, N. Li, Z.-Q. Liu, Rational design and synthesis of hollow Fe–N/C electrocatalysts for enhanced oxygen reduction reaction, Chem Commun 57 (2021) 5258–5261.

[32] Y. Zhao, F. Zhao, X. Wang, C. Xu, Z. Zhang, G. Shi, L. Qu, Graphitic carbon nitride nanoribbons: graphene-assisted formation and synergic function for highly efficient hydrogen evolution, Angew Chem Int Edit 53 (2014) 13934–13939.

[33] Y. Zheng, Y. Jiao, Y. Zhu, L.H. Li, Y. Han, Y. Chen, A. Du, M. Jaroniec, S.Z. Qiao, Hydrogen evolution by a metal-free electrocatalyst, Nat Commun 5 (2014) 3783.

[34] F. Zhen-Yi, L. Yu-Xian, Effective Route to Graphitic carbon Nitride from Ball-Milled Amorphous carbon in NH 3 Atmosphere Under Annealing, Chin Phys Lett 20 (2003) 1554–1557.

[35] I. Boukhoubza, M. Khenfouch, M. Achehboune, B.M. Mothudi, I. Zorkani, A. Jorio, X-ray diffraction investigations of nanostructured ZnO coated with reduced graphene oxide, J. Phys.: Conf. Ser. , 1292 (2019) 012011.

[36] H.S. Maharana, P.K. Rai, A. Basu, Surface-mechanical and electrical properties of pulse electrodeposited Cu-graphene oxide composite coating for electrical contacts, J Mater Sci 52 (2017) 1089–1105.

[37] A. Kumar, A.M. Sadanandhan, S.L. Jain, Silver doped reduced graphene oxide as a promising plasmonic photocatalyst for oxidative coupling of benzylamines under visible light irradiation, New J Chem 43 (2019) 9116–9122.

[38] A. Jabbar, G. Yasin, W.Q. Khan, M.Y. Anwar, R.M. Korai, M.N. Nizam, G. Muhyodin, Electrochemical deposition of nickel graphene composite coatings:

effect of deposition temperature on its surface morphology and corrosion resistance, RSC Adv 7 (2017) 31100–31109.

[39] F. Nichols, Q.M. Liu, J. Sandhu, Z. Azhar, R. Cazares, R. Mercado, F. Bridges, S.W. Chen, Platinum-complexed phosphorous-doped carbon nitride for electrocatalytic hydrogen evolution, J Mater Chem A 10 (2022) 5962–5970.

[40] C.H. Zhang, J.W. Sha, H.L. Fei, M.J. Liu, S. Yazdi, J.B. Zhang, Q.F. Zhong, X.L. Zou, N.Q. Zhao, H.S. Yu, Z. Jiang, E. Ringe, B.I. Yakobson, J.C. Dong, D.L. Chen, J.M. Tour, Single-Atomic Ruthenium Catalytic Sites on Nitrogen-Doped Graphene for Oxygen Reduction Reaction in Acidic Medium, Acs Nano 11 (2017) 6930–6941.

[41] J. Yang, D. He, W. Chen, W. Zhu, H. Zhang, S. Ren, X. Wang, Q. Yang, Y. Wu, Y. Li, Bimetallic Ru-Co Clusters Derived from a Confined Alloying Process within Zeolite-Imidazolate Frameworks for Efficient NH3 Decomposition and Synthesis, Acs Appl Mater Interfaces 9 (45) (2017) 39450–39455.